

Article

# A Combined Mechanochemical and Calcination Route to Mixed Cobalt Oxides for the Selective Catalytic Reduction of Nitrophenols

Lorianne R. Shultz<sup>1,2</sup>, Bryan McCullough<sup>1,3</sup>, Wesley J. Newsome<sup>1</sup> , Haider Ali<sup>4</sup>,  
Thomas E. Shaw<sup>1,2</sup>, Kristopher O. Davis<sup>4,5</sup>, Fernando J. Uribe-Romo<sup>1,2,\*</sup>,  
Matthieu Baudalet<sup>1,3,5,\*</sup> and Titel Jurca<sup>1,2,6,\*</sup>

<sup>1</sup> Department of Chemistry, University of Central Florida, 4111 Libra Drive, Orlando, FL 32816, USA; lorishultz@knights.ucf.edu (L.R.S.); mcculloughbp21@knights.ucf.edu (B.M.); wesnewsome@knights.ucf.edu (W.J.N.); tshaw@knights.ucf.edu (T.E.S.)

<sup>2</sup> Renewable Energy and Chemical Transformations Cluster, University of Central Florida, 4353 Scorpius Street, Orlando, FL 32816, USA

<sup>3</sup> National Center for Forensic Science, University of Central Florida, 12354 Research Parkway #225, Orlando, FL 32826, USA

<sup>4</sup> Department of Materials Science and Engineering, University of Central Florida, Orlando, FL 32816, USA; alihaidar@knights.ucf.edu (H.A.); Kristopher.Davis@ucf.edu (K.O.D.)

<sup>5</sup> CREOL—The College of Optics & Photonics, Building 53, University of Central Florida, 4304 Scorpius Street, Orlando, FL 32816, USA

<sup>6</sup> NanoScience Technology Center, University of Central Florida, Orlando, FL 32826, USA

\* Correspondence: fernando@ucf.edu (F.J.U.-R.); baudalet@ucf.edu (M.B.); titel.jurca@ucf.edu (T.J.)

Academic Editor: Ali Nazemi

Received: 26 November 2019; Accepted: 15 December 2019; Published: 25 December 2019



**Abstract:** Para-, or 4-nitrophenol, and related nitroaromatics are broadly used compounds in industrial processes and as a result are among the most common anthropogenic pollutants in aqueous industrial effluent; this requires development of practical remediation strategies. Their catalytic reduction to the less toxic and synthetically desirable aminophenols is one strategy. However, to date, the majority of work focuses on catalysts based on precisely tailored, and often noble metal-based nanoparticles. The cost of such systems hampers practical, larger scale application. We report a facile route to bulk cobalt oxide-based materials, via a combined mechanochemical and calcination approach. Vibratory ball milling of  $\text{CoCl}_2(\text{H}_2\text{O})_6$  with KOH, and subsequent calcination afforded three cobalt oxide-based materials with different combinations of  $\text{CoO}(\text{OH})$ ,  $\text{Co}(\text{OH})_2$ , and  $\text{Co}_3\text{O}_4$  with different crystallite domains/sizes and surface areas;  $\text{Co}@100$ ,  $\text{Co}@350$  and  $\text{Co}@600$  ( $\text{Co}@###$ ; # = calcination temp). All three prove active for the catalytic reduction of 4-nitrophenol and related aminonitrophenols. In the case of 4-nitrophenol,  $\text{Co}@350$  proved to be the most active catalyst, therein its retention of activity over prolonged exposure to air, moisture, and reducing environments, and applicability in flow processes is demonstrated.

**Keywords:** nitroaromatics; catalytic reduction; metal oxide catalysis; waste valorization; water chemistry; nanocatalysis

## 1. Introduction

Para-, or 4-nitrophenol (4NP), and more broadly, compounds in the nitroaromatic family are widely used in the industrial fabrication of pharmaceuticals, explosives, pesticides, pigments, and dyes [1–4]. As a result, nitroaromatics have become a very common anthropogenic pollutant arising from aqueous industrial effluent. While many nitroaromatics have been shown to display acute toxicity,

are mutagenic, and either potential or established carcinogens [5–7], their reduction products, aniline derivatives, are typically less toxic, commercially important synthetic intermediates. For example, the reduction product of 4NP is 4-aminophenol (4AP); a useful component for the synthesis of dyes, agrochemicals, and pharmaceuticals [8–11]. As a result, the aqueous catalytic reduction of 4NP has emerged as an important research area (Figure 1) [12]. Due to its concomitant use as a probe reaction system for heterogeneous catalyst development, a majority of this work, to date, has focused on noble metal nanoparticles (e.g., Au, Pt, Pd, etc.) [13–15]. However, although this chemistry is effectively developed with noble metal nanoparticles [16–29], their cost precludes practical scaled-up implementation. As a result, a number of methods utilizing materials that are either based on Earth-abundant metals [30–38] or are metal free [39–46] have emerged. Therein, cobalt oxide nanoparticles have drawn significant interest as active, low-cost alternatives to the noble metal systems [47–52]. Such species are prepared by solution-based routes commensurate with conventional nanoparticle synthesis. Although promising, the effort required for precise nanoparticle preparation can be inhibitory towards practical larger-scale applications.

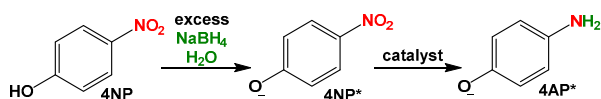


**Figure 1.** Catalytic reduction of 4-nitrophenol (4NP) to 4-aminophenolate (4AP\*).

Herein, we report a facile route to bulk cobalt oxide-based materials, via vibratory ball milling [53] and subsequent calcination. Vibratory ball milling, utilizing the SPEX<sup>®</sup> 8000 model, as used for herein, draws ca. 249 W, comparatively, a standard hot plate stirrer draws ca. 10 W for stirring alone, and peaks at 1.5 kW to maintain a modest temperature of 80 °C, commensurate with milder hydrothermal processes for nanoparticle synthesis. By taking into consideration that mechanochemical processes are typically conducted over a shorter time span than conventional solution processes, the energy savings become additive, thus, enhancing sustainability [54]. Furthermore, the process utilizes inexpensive starting materials, no solvent during synthesis, and only deionized water (DIW) for workup. The bulk material, calcined at three different temperatures (100, 350, and 600 °C) respectively denoted as Co@100, Co@350 and Co@600, and composed of increasing amounts of Co<sub>3</sub>O<sub>4</sub> as a function of temperature, displays different catalytic activity, and surprisingly different selectivity when utilized for the reduction of 4NP, and several aminonitrophenols. All catalytic rates observed are competitive with related literature process. The most active catalyst, Co@350 as deduced from 4NP reduction trials (vide infra) is robust, air and moisture resistant, displaying longevity, excellent recyclability, and applicability in flow processes. Paired with the ease of synthesis, and the inherent scalability of mechanochemical processes [55–63], these results are promising for the development of inexpensive, robust, and sustainable bulk catalysts capable of reducing nitrophenol pollutants in aqueous media.

## 2. Results and Discussion

### 2.1. Catalyst Synthesis

In a tungsten carbide (WC) vial, CoCl<sub>2</sub>(H<sub>2</sub>O)<sub>6</sub> (4.2 mmol, 1.0 g) was mixed with excess KOH (89 mmol, 5 g) and (2×) 11.2 mm WC balls. The vessel was sealed, and placed on a SPEX<sup>®</sup> 8000 mill and allowed to react for 2 h after which point it was opened and the dark brown powder washed with 100 mL of DIW, passed through a medium glass filter frit to remove large particulates, and centrifuged at 3500 rpm for 3 min. to afford a dark bronze solid. The solid was dried in vacuo at 100 °C for 4 h to remove the remaining H<sub>2</sub>O, yielding 387 mg of dark brown/black powder. The resulting powder was split in three (129 mg each), one portion was kept “as synthesized” (Co@100) and the remaining two heated to 350 °C (110 °C h<sup>-1</sup> for 3 h, hold 2 h at 350 °C) and 600 °C (110 °C h<sup>-1</sup> for 5 h, hold 2 h at 600 °C), respectively (Co@350 and Co@600, Figure 2). Unless otherwise noted, samples were stored in sealed vials in a desiccator (10% RH).

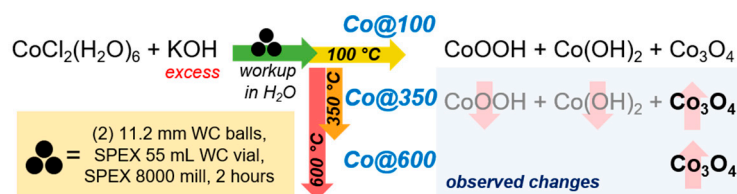


**Figure 2.** General protocol for the preparation of Co@100, Co@350, and Co@600.

## 2.2. Catalyst Characterization

Scanning electron microscopy (SEM) of the powders in each instance revealed an amorphous agglomeration of micron-sized particles of compacted material decorated in highly dispersed nano-to-micron sized semi-spherical clusters (Figure 3A–C and Figure S1) [64–66]. The large agglomerates are attributed to the impacts from the preparative method. Energy dispersive X-ray spectroscopy (EDX) confirms the presence of Co as the predominant species, with residual K from the milling process (Figure S1). Transmission electron microscopy (TEM) of all three samples after prolonged sonication in methanol at 40 °C, to enable decomposition of the micron-sized agglomerates, reveals agglomerated nanoplates ranging anywhere between <10 nm to >50 nm (Figure 3D–F and Figure S2). Nanoplate definition is greatly enhanced for Co@600 (Figure 3F), commensurate with higher crystallinity and formation of a predominantly single Co-oxide species (vide infra).

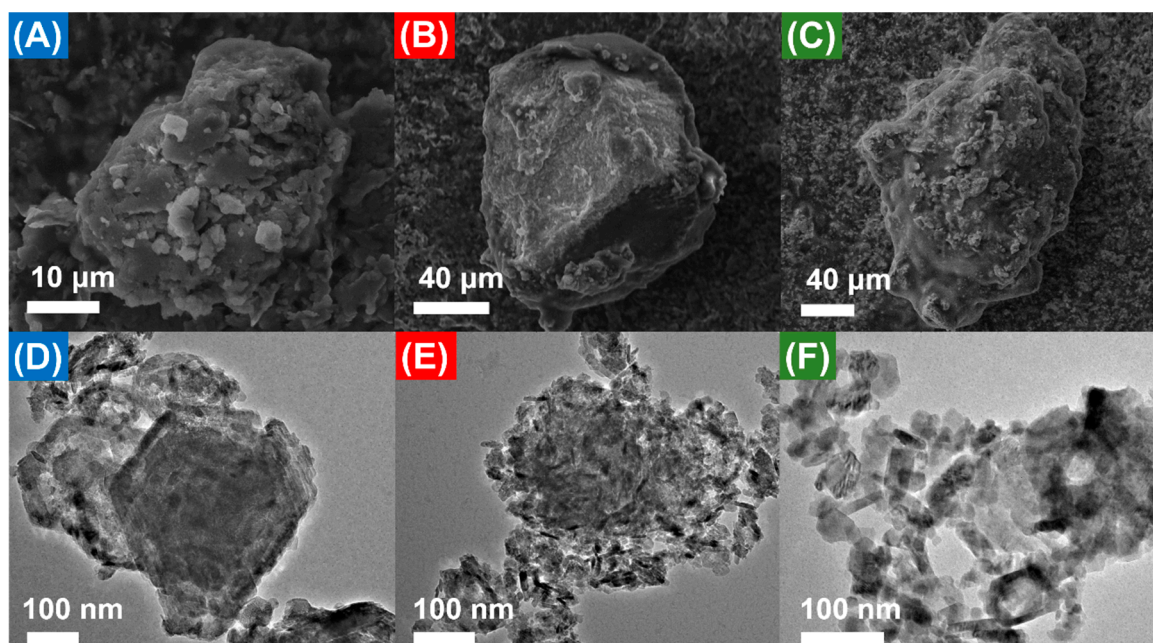


**Figure 3.** Representative SEM images of Co@100 (A), Co@350 (B), and Co@600 (C), and representative TEM images of Co@100 (D), Co@350 (E) and Co@600 (F) after sonication.

Raman spectroscopy of Co@100 (Figure 4A and Figure S3) was indicative of the presence of  $\text{Co}_3\text{O}_4$  with characteristic peaks at 198, 491, 528, 624, and 694  $\text{cm}^{-1}$  corresponding to the  $\text{F}_{2g}$ ,  $\text{E}_g$ ,  $\text{F}_{2g}$ ,  $\text{F}_{2g}$ , and  $\text{A}_{1g}$  modes, respectively [67,68]. However, the region of 450 to 650  $\text{cm}^{-1}$  is sufficiently broadened and raised above the baseline. Broad peaks in this region are characteristic for  $\text{CoO}(\text{OH})$  and  $\text{Co}(\text{OH})_2$ , both of which exhibit peaks at ca. 500  $\text{cm}^{-1}$  corresponding to  $\text{E}_g$  and  $\text{A}_{2u}$  modes. Additionally, they both feature very broad peaks centered at ca. 600  $\text{cm}^{-1}$  corresponding to the  $\text{A}_{1g}$  and  $\text{E}_g$  modes of  $\text{CoO}(\text{OH})$  and  $\text{Co}(\text{OH})_2$ , respectively. The spectrum of Co@100 reveals multiple overlapping signals at both 497 and 505  $\text{cm}^{-1}$ , as well as very broad signals over the entire area of interest; likely due to the presence of both  $\text{Co}(\text{OH})_2$  and  $\text{CoO}(\text{OH})$  [67–70]. Going from Co@100 to Co@350 and Co@600, the peaks assigned to  $\text{Co}(\text{OH})_2$  and  $\text{CoO}(\text{OH})$  gradually disappear giving way to sharper features at

198, 482, 519, 621, and 693  $\text{cm}^{-1}$  (Co@600) corresponding to the  $F_{2g}$ ,  $E_g$ ,  $F_{2g}$ ,  $F_{2g}$ , and  $A_{1g}$  of  $\text{Co}_3\text{O}_4$ , indicating near complete conversion to the mixed oxide [67,68,71]. Additional broad features at  $\sim 130$  to  $300 \text{ cm}^{-1}$  are attributed to the presence of residual KOH (Figure S3).

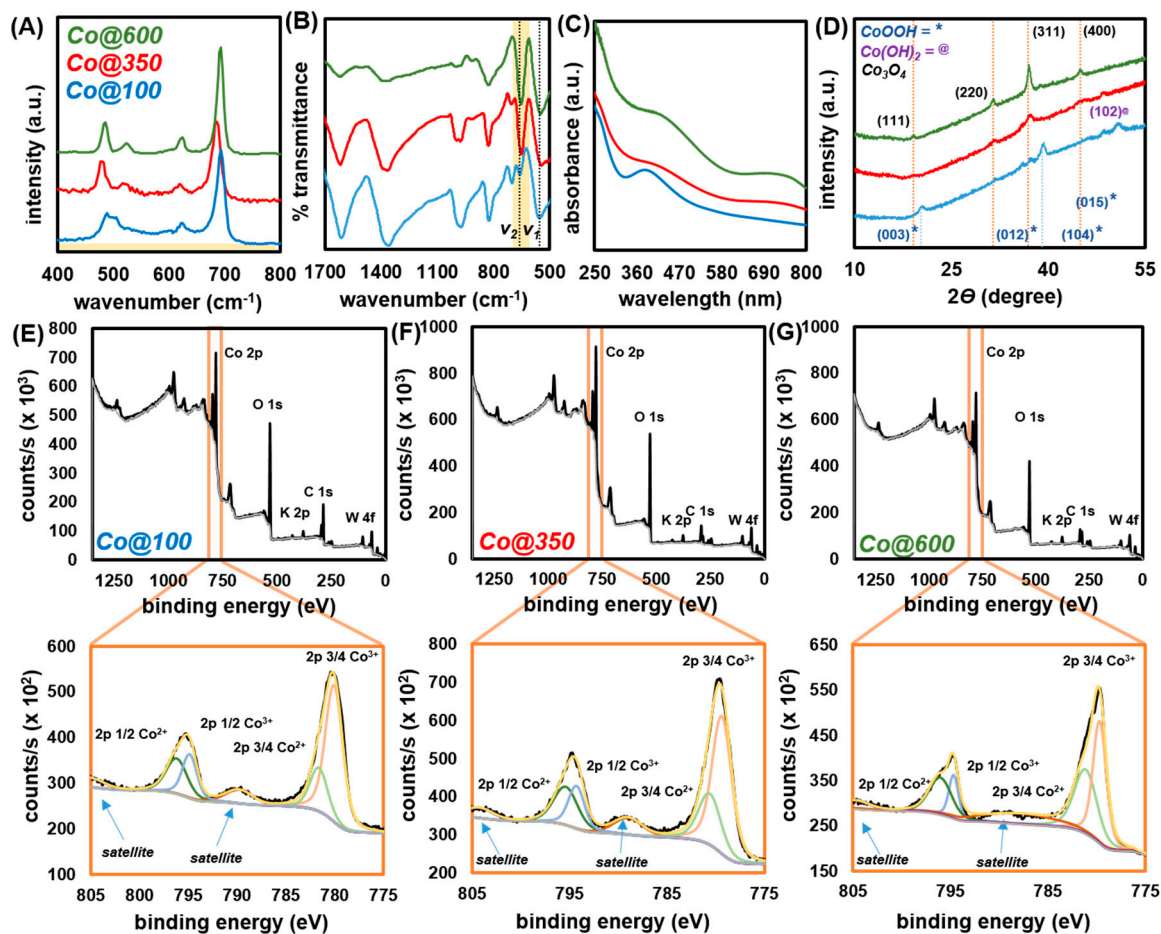


**Figure 4.** Raman (A), FTIR (B), UV-Vis (C), and XRD (D) spectra of Co@100, Co@350 and Co@600. (a.u. = arbitrary units). XPS survey and close-up of Co 2p region for (E) Co@100, (F) Co@350, and (G) Co@600.

FTIR of Co@100 reveals a very broad high intensity peak at ( $v_1$ )  $551 \text{ cm}^{-1}$  and a sharp lower intensity peak at ( $v_2$ )  $659 \text{ cm}^{-1}$  (Figure 4B and Figure S2). Notably,  $v_1$  is likely a combination of vibration modes for Co-O in  $\text{Co}_3\text{O}_4$  spinel ( $\text{Co}^{3+}$ ), in  $\text{CoO(OH)}$ , and in  $\text{Co(OH)}_2$  [72–76]. The sharp lower intensity  $v_2$  is attributed to the vibration of Co-O in  $\text{Co}_3\text{O}_4$  spinel ( $\text{Co}^{2+}$ ), which increases in intensity as calcination temperature increases (Co@350 and Co@600). Additional broad peaks associated with respective surface hydroxides,  $\text{H}_2\text{O}$  (very broad at  $1614 \text{ cm}^{-1}$ ) [77], and carboxylates ( $\text{COO}^-$ , at  $1614 \text{ cm}^{-1}$  and  $1360 \text{ cm}^{-1}$ ) [78] adsorbed and formed during handling and storage in ambient, and residual KOH from the milling process (vide supra) are also present. However, their complexity makes a clear assignment difficult. The UV-Vis spectrum of Co@100 (Figure 4C) in DIW features a broad peak at  $\lambda_{\text{max}} = 390 \text{ nm}$ , characteristic of  $\text{CoO(OH)}$ ; but may also be attributed to the presence of  $\beta\text{-Co(OH)}_2$  [73,79]. There is significant, however ill-defined absorbance up to the as measured  $800 \text{ nm}$  region, which is attributed to the presence of  $\text{Co}_3\text{O}_4$  in accordance to observations from both Raman and FTIR. Going from Co@100, to Co@350 and Co@600, the peak at  $\lambda_{\text{max}} = 390 \text{ nm}$  disappears, giving way to the progressively better-defined broad bands at ca.  $\lambda_{\text{max}} = 430 \text{ nm}$  and  $\lambda_{\text{max}} = 740 \text{ nm}$ , attributed to the ligand-metal charge transfer events  $\text{O} \rightarrow \text{Co}^{2+}$  and  $\text{O} \rightarrow \text{Co}^{3+}$  of  $\text{Co}_3\text{O}_4$ , respectively [80].

Powder X-ray diffraction (Figure 3D) of Co@100 reveals the presence of mainly CoO(OH), with observable small amounts of Co(OH)<sub>2</sub>; confirmed by Raman (Figure 4D). The CoO(OH) phase appears with broad peaks (FWHM = 0.74), characteristic of the small domain size of the crystallites. Calcination to Co@350 results in phase transformation to nanocrystalline Co<sub>3</sub>O<sub>4</sub> (spinel) with trace amounts of CoO(OH) and Co(OH)<sub>2</sub>. Calcination at 600 °C resulted in Co@600 with a PXRD pattern that displays sharp diffraction lines of Co<sub>3</sub>O<sub>4</sub> (spinel) and complete disappearance of the hydroxide phases. These observations are commensurate with the spectroscopic observations. The porosity of the particles was analyzed utilizing N<sub>2</sub> gas adsorption at 77 K (Figure S3). All three compounds exhibit an IUPAC type II isotherm, characteristic of microporous materials with multilayer adsorption. The hysteresis observed at high pressure accentuates the difference in the adsorption/desorption mechanism characteristic of porous oxide materials [81]. Application of the Brunauer-Emmet-Teller (BET) model over the low-pressure region (up to 0.1  $p/p_0$ ) resulted in BET surface areas of  $S_{\text{BET}} = 21.75, 28.48, 10.38 \text{ m}^2 \text{ g}^{-1}$  for Co@100, Co@350, and Co@600 (Figure S4).

X-ray photoelectron spectroscopy (XPS) was carried out on all three samples. As expected, measurements confirmed the majority constituents to be Co, O, and C, with a minor contaminant of K and <2% W attributed to residue from the WC grinding implements (Figure 4E–G). The presence of C is ascribed to the presence of hydrocarbon contaminants (Figure S5) [82,83]. Critical to the assessment of the material are the Co 2p peaks which reveal the ratio of Co<sup>2+</sup> to Co<sup>3+</sup> in the system. The observed peaks at respective binding energies (eV) and correlated % Co<sup>2+/3+</sup> compositions are as follows: Co@100 2p<sub>1/2</sub> (Co<sup>2+</sup>) 796.6 eV, 2p<sub>1/2</sub>(Co<sup>3+</sup>) 795.4 eV, 2p<sub>3/4</sub> (Co<sup>2+</sup>) 781.6 eV, 2p<sub>3/4</sub> (Co<sup>3+</sup>) 780.1 eV, Co<sup>2+</sup> = 23.9%, and Co<sup>3+</sup> = 76.1%; Co@350 2p<sub>1/2</sub> (Co<sup>2+</sup>) 795.5 eV, 2p<sub>1/2</sub>(Co<sup>3+</sup>) 794.2 eV, 2p<sub>3/4</sub> (Co<sup>2+</sup>) 780.6 eV, 2p<sub>3/4</sub> (Co<sup>3+</sup>) 779.4 eV, Co<sup>2+</sup> = 30.0%, and Co<sup>3+</sup> = 70.0%; Co@600 2p<sub>1/2</sub> (Co<sup>2+</sup>) 796.6 eV, 2p<sub>1/2</sub>(Co<sup>3+</sup>) 794.8 eV, 2p<sub>3/4</sub> (Co<sup>2+</sup>) 781.2 eV, 2p<sub>3/4</sub> (Co<sup>3+</sup>) 779.7 eV, Co<sup>2+</sup> = 47.7%, and Co<sup>3+</sup> = 52.3%. Thus, the compositions support the transition from predominantly CoO(OH) (Co<sup>3+</sup>) to predominantly Co<sub>3</sub>O<sub>4</sub> (2:1 Co<sup>3+</sup>:Co<sup>2+</sup>) [64,84,85]. The “overshoot” in Co<sup>2+</sup> content for Co@600 is potentially due to a combination of surface –OH sites or oxygen vacancies arising from the preparative process and handling under high humidity ambient conditions.

Combining the spectroscopic, diffraction, and porosity measurements, thermal treatment of cobalt-based nanoparticles first induces a structural rearrangement from mainly cobalt oxyhydroxide to a mixed system featuring both oxyhydroxide and spinel with small crystallite size and increased accessible surface area. Annealing at 600 °C results in increased particle size with a decrease in surface area with formation of predominantly Co<sub>3</sub>O<sub>4</sub> spinel, with likely oxygen vacancies or amorphous surface hydroxides. The change in chemical environment is echoed by the initial decreased (red) shift (Co@100 to Co@350) then increased (blue) shift (Co@350 to Co@600) observed by Raman (Figure 4A).

### 2.3. Catalysis

#### 2.3.1. Catalytic Reduction of 4-Nitrophenol

To investigate the catalytic performance of Co@100, Co@350 and Co@600, 4-nitrophenol (4NP) reduction reactions were conducted in a standard 1 cm path length quartz UV cell and monitored in the 225 to 475 nm region, under ambient (21 °C). In a typical reaction, 0.39 μmol 4NP was diluted in 1 mL DIW mixed with a 2 mL solution of 0.2 mmol NaBH<sub>4</sub> (pH 10.46); this initial reaction generates 4-nitrophenolate (4NP\*) marked by a color change from pale to bright yellow, and a red shift from  $\lambda_{\text{max}} = 317 \text{ nm}$  to  $\lambda_{\text{max}} = 400 \text{ nm}$  (Figure 5, Figure 6 and Figure S6). After the  $t_0$  absorbance was recorded, 1 mg of catalyst was added and stirred for ~2 s. The reaction was monitored at fixed intervals by the decreasing absorbance at  $\lambda_{\text{max}} = 400 \text{ nm}$ . This was accompanied by the appearance of a lower intensity peak at  $\lambda_{\text{max}} = 310 \text{ nm}$ , consistent with 4-aminophenolate (4AP\*); 4-aminophenol (4AP) appears at ca.  $\lambda_{\text{max}} = 300 \text{ nm}$  (Figure S6). Practically, this denotes a color change from bright yellow to colorless. Notably, all three catalysts promote hydrolysis of NaBH<sub>4</sub> resulting in a turbid solution and an artificially increased baseline absorbance (~1 a.u.). The catalytic hydrolysis of NaBH<sub>4</sub> by Co<sub>3</sub>O<sub>4</sub>-based

species has been previously reported, and therefore it is not surprising that a similar competing reaction is operating herein [86–88]. To effectively extract data under these conditions, the resulting spectra were normalized to an isosbestic point at 250 nm.

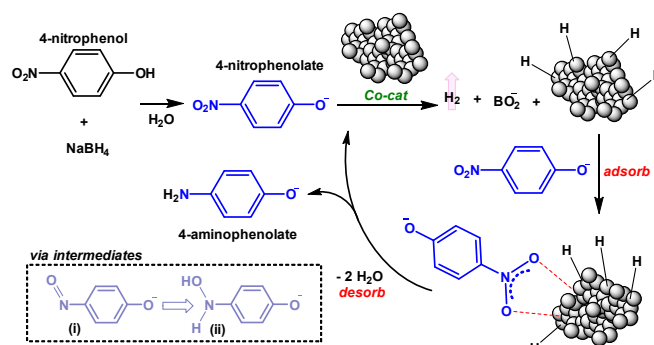


**Figure 5.** Proposed general mechanism for the reduction of 4NP with catalysts Co@100, Co@350, and Co@600 in H<sub>2</sub>O with excess NaBH<sub>4</sub>.

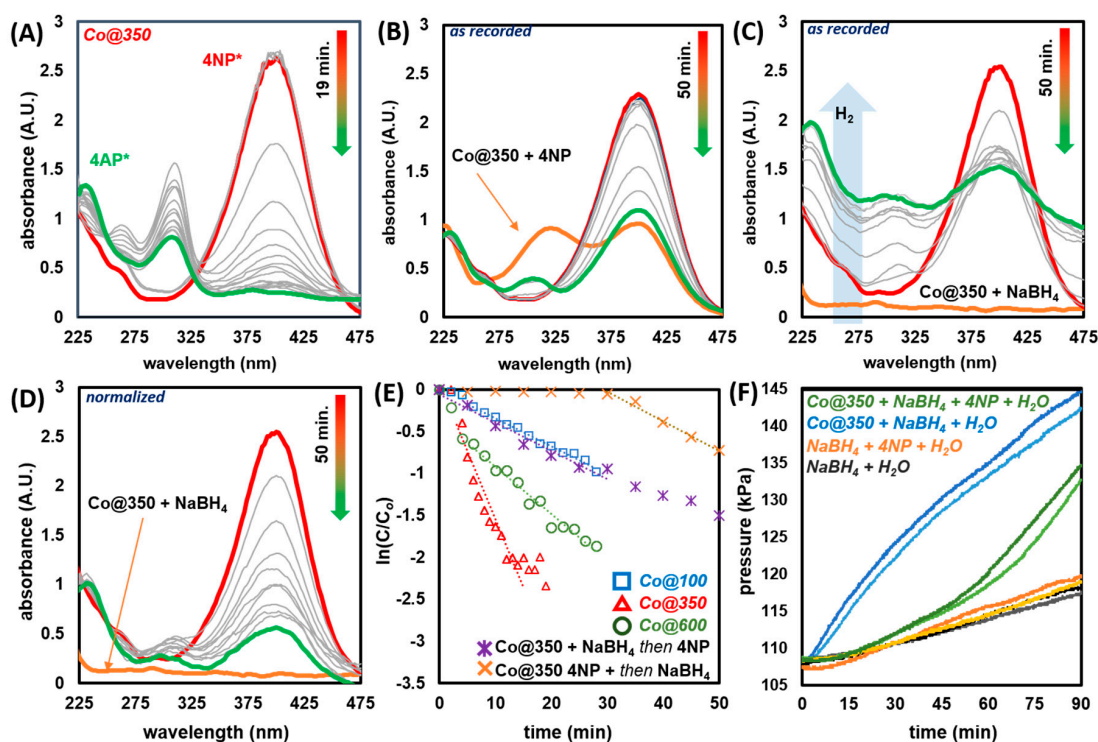


**Figure 6.** (A) UV-Vis spectra for the reduction of 4NP by Co<sub>350</sub>; (B) Co@350 and 4NP, dwell 5 min, then, NaBH<sub>4</sub> addition; (C) Co@350 and NaBH<sub>4</sub>, dwell 5 min, then 4NP addition; (D) spectrum (C) normalized at 250 nm; (E) plot of ln(C/C<sub>0</sub>) as a function of time; and (F) change in pressure associated with the evolution of H<sub>2</sub> in closed system (repeat trials shown).

When conducted in the presence of excess NaBH<sub>4</sub>, the reaction is commonly described in terms of the Langmuir-Hinshelwood model [13,89–91]. According to the model, reactants 4NP\* and NaBH<sub>4</sub> derived surface hydrogen are first adsorbed onto the catalyst surface in a fast and reversible process. Following an induction period (vide infra), the reaction proceeds according to pseudo-first order kinetics, via intermediates 4-nitrosophenol and 4-hydroxylaminophenol (Figure 5i,ii) [92–94] ultimately yielding the product 4AP\*, which rapidly desorbs from the surface, thus bearing minimal impact on the overall kinetics (Figure 5). As a result, the rate-limiting step can be described as the reaction of adsorbed 4NP and hydrogen on the catalyst surface. Thus, the resulting catalyst performance is quantified in terms of the apparent rate constant  $k_{app}$  (Equation), derived from the slope of ln(C/C<sub>0</sub>) as a

function of time;  $C/C_0$  is obtained from the absorbance for 4NP\* at  $\lambda_{\max} = 400$  nm ( $A/A_0$ ), collected after an induction period (vide infra). The details governing this approximation have been discussed in prior literature [5].

$$-k_{app}t = \ln\left(\frac{A}{A_0}\right) = \ln\left(\frac{C}{C_0}\right)$$

Reactions promoted by all three catalysts, monitored at 2 min intervals, proceeded as expected (Figure 6A and Figure S5). Reactivity, as delineated by  $k_{app}$  was found to proceed in the order Co@350 ( $0.189 \text{ min}^{-1}$ ) > Co@600 ( $0.057 \text{ min}^{-1}$ ) > Co@100 ( $0.033 \text{ min}^{-1}$ ) (Figure 6F, Table 1). By comparison, repeating the reaction with commercial  $\text{Co}_3\text{O}_4$  led to no observed reaction over the 50 min period tested (Figure S8A). Because all three catalysts feature a different composition of materials, a comparative analysis of structure-activity relationships is not possible. Within the context of Co@600, enhanced activity over pristine commercially sourced  $\text{Co}_3\text{O}_4$  can be attributed to the presence of oxygen vacancies. Chen and coworkers have previously reported oxygen vacancy enhanced activity of  $\text{Co}_3\text{O}_4$  towards 4NP reduction, wherein pristine  $\text{Co}_3\text{O}_4$  exhibited long induction periods and low initial activity, whereas reduced species, denoted by higher  $\text{Co}^{2+}$  content by XPS, were more active [50]. Co@600 exhibits a Co composition of  $\text{Co}^{2+}:\text{Co}^{3+}$  47.7%:52.3% as compared with  $\text{Co}_3\text{O}_4$  (1:2  $\text{Co}^{2+}:\text{Co}^{3+}$ ). The exact blend of  $\text{CoO}(\text{OH})$ ,  $\text{Co}_3\text{O}_4$ , surface  $\text{Co}(\text{OH})_2$ , and relative oxygen vacancies of Co@100 and Co@350 are difficult to assign, thus their activity can more broadly be attributed to the process-specific mixture of the aforementioned components. Therein, the processing parameters leading to Co@350 yield the most active mixed cobalt oxide blend for 4NP reduction. However, Co@600 exhibits larger crystallite/domain size and decreased BET surface area (Co@350 =  $28.28 \text{ m}^2 \text{ g}^{-1}$  and Co@600 =  $10.38 \text{ m}^2 \text{ g}^{-1}$ ), which may account for the increased  $k_{app}$  of Co@350.

**Table 1.** Summary of catalytic trials.

Cat.	Substrate.	Change	$k_{app}$ ( $\text{min}^{-1}$ )	Induction (min)
–	4NP	–	no rxn	–
Co@100	4NP	–	0.033	2
Co@350	4NP	–	0.189	2
Co@600	4NP	–	0.057	<2
Co@100	4NP	no $\text{NaBH}_4$	no rxn	–
Co@350	4NP	no $\text{NaBH}_4$	no rxn	–
Co@600	4NP	no $\text{NaBH}_4$	no rxn	–
Co@350	4NP	+1 mg KOH	0.132	1
Co@350	4NP	+ $\text{NaBH}_4$ last	0.035	30
Co@350	4NP	+4NP last	0.032	<5
KOH	4NP	–	no rxn	–
$\text{Co}_3\text{O}_4$	4NP	–	no rxn	–
Co@100	4A3NP	–	0.004	30
Co@350	4A3NP	–	0.114	6
Co@600	4A3NP	–	0.003	16
Co@100	2A5NP	–	0.047/0.175	8
Co@350	2A5NP	–	0.143	28
Co@600	2A5NP	–	0.264	22

A direct comparison to literature catalysts is complicated by the dependence of  $k_{app}$  on multiple factors including  $\text{NaBH}_4$  concentration, mass transport, reaction volume, catalyst weight, temperature, and the nature and density of active sites, which in most cases, ours included, remain enigmatic. Nonetheless, it is accepted that  $k_{app}$  normalized to reaction volume and catalyst mass, dubbed “activity parameter”  $\kappa$  ( $\text{s}^{-1} \text{ g}^{-1} \text{ L}$ ) can facilitate a useful comparison [95,96]. Using these parameters, Co@350 exhibits a  $\kappa$  value of  $9.5 \times 10^{-3} \text{ s}^{-1} \text{ g}^{-1} \text{ L}$ . This is comparable to a number of recent literature reports for both metal oxides; CuO ( $6.2 \times 10^{-3} \text{ s}^{-1} \text{ g}^{-1} \text{ L}$ ), [7c]  $\text{Co}_3\text{O}_4$  ( $4.2 \times 10^{-3} \text{ s}^{-1} \text{ g}^{-1} \text{ L}$ ) [32], and meso- $\text{Co}_3\text{O}_4$  ( $3.8 \times 10^{-3} \text{ s}^{-1} \text{ g}^{-1} \text{ L}$ ) [48]; metal nanoparticles Ni ( $2.9 \times 10^{-3} \text{ s}^{-1} \text{ g}^{-1} \text{ L}$ ) [97], Ni on

carbon ( $27.6 - 69.6 \times 10^{-3} \text{ s}^{-1} \text{ g}^{-1} \text{ L}$ ) [98], and Au on  $\text{Fe}_3\text{O}_4$  ( $61.0 \times 10^{-3} \text{ s}^{-1} \text{ g}^{-1} \text{ L}$ ) [99]; and metal free catalysts such as sulfurized graphene ( $6.2 \times 10^{-3} \text{ s}^{-1} \text{ g}^{-1} \text{ L}$ ) [46].

To confirm adherence to the Langmuir-Hinshelwood model [13,89–91], two additional experiments were conducted with Co@350 utilizing similar parameters as detailed prior, while altering the order of reagent addition. First, Co@350 and 4NP in DIW were introduced to the quartz cell and absorbance was recorded (Figure 6B). Notably some 4NP is immediately converted to 4NP\* (normally a slower process); this is observed for all three catalysts (Figure S7) and is attributed to the presence of residual KOH. After the initial measurement,  $\text{NaBH}_4$  is added to the system and absorbance is subsequently measured at 5 min intervals. With this sequence of addition, there is a considerable induction time (30 min) during which negligible  $\text{H}_2$  evolution is observed; this is evident by the lack of turbidity of the solution which reveals no increase in baseline absorbance in the recorded spectrum (Figure 6B). The process was repeated with initial introduction of Co@350 and  $\text{NaBH}_4$  in DIW, measurement of absorbance and subsequent addition of 4NP with monitoring at 5 min intervals. In this instance,  $\text{H}_2$  evolution was immediately noticeable, and reflected in the recorded spectra which featured a dramatically increased baseline absorbance (Figure 6C, normalized values see Figure 6D). Notably, there was no observed induction time at 5 min. The reactions proceeded with a  $k_{app}$  of  $0.035 \text{ min}^{-1}$  (Co@350 + 4NP then  $\text{NaBH}_4$ ) and  $0.032 \text{ min}^{-1}$  (Co@350 +  $\text{NaBH}_4$ , then 4NP), indicating that the reduction process is likely similar post induction period. Ultimately, it appears the optimal scenario is the introduction of catalyst to a mixture of  $\text{NaBH}_4$  and preformed 4NP\*, which in the case of Co@350 resulted in a  $k_{app}$  of  $0.189 \text{ min}^{-1}$  with minimal induction time (2 min).

4NP has been shown to have a dramatically higher adsorption constant than  $\text{BH}_4^-$  for  $\text{Co}_3\text{O}_4$  ( $K_{4NP} = 922 \pm 40 \text{ L mol}^{-1}$  and  $K_{\text{BH}_4^-} = 22 \pm 4 \text{ L mol}^{-1}$ ) [48]. This is consistent with our observed induction period (30 min), where initial exposure to 4NP likely results in complete coverage of catalyst surface sites, thereby preventing co-adsorbance of  $\text{BH}_4^-$  necessary to generate the surface hydrogens (which readily evolve  $\text{H}_2$ ) required for catalytic turnover. Alternatively, initial formation of surface hydrogen species does not fully out-compete 4NP adsorption even if addition is delayed, and the reaction proceeds without significant induction time, and with similar rate. This is consistent with the Langmuir-Hinshelwood model which necessitates adsorption of both species onto the catalyst surface prior to reaction [13,89–91]. These findings can also rule out the competing Eley-Rideal mechanism [100–102], which is predicated on the collision of substrate with surface-bound hydrogens; in such a case we would expect our second scenario (Co@350 +  $\text{NaBH}_4$  then 4NP), featuring a hydrogen rich surface and all 4NP initially in the solution state to have exhibited an enhanced  $k_{app}$ .

In a separate experiment, the change in pressure associated with the hydrolysis of  $\text{NaBH}_4$  as promoted by Co@350 both in the absence and in competition with 4NP was monitored in a closed system (Figure 6F and Figure S9). In the absence of catalyst, the pressure of the system changes by  $\Delta 9.27 \text{ kPa}$  over 90 min. due to slow hydrolysis of  $\text{NaBH}_4$  in  $\text{H}_2\text{O}$ . Introduction of Co@350 results in enhanced  $\text{H}_2$  production, resulting in an additional pressure change of  $\Delta 25.59 \text{ kPa}$ . Overall this represents a nearly four-fold increase in hydrolysis rate, as expected for Co-based catalysts [87–89]. Monitoring the pressure change for the reduction of 4NP in the system reveals only slight deviation over the first ~50 min (4NP reduction period). After this point, pressure begins to increase steadily with a similar slope as observed for trials in the presence of Co@350, and the absence of 4NP. These observations are consistent with the higher adsorption constant for 4NP vs.  $\text{BH}_4^-$  with  $\text{Co}_3\text{O}_4$  [48] and further validate the mechanistic studies outlined in Figure 6B–D (vide supra) [13,89–91]. Moreover, commercial  $\text{Co}_3\text{O}_4$  readily promotes  $\text{NaBH}_4$  hydrolysis [88], although it fails to promote 4NP reduction during the time tested (Figure S8B), thus validating that (a) it is not fully passivated and capable of being catalytically active, and (b) that the preparative routes undertaken for our materials yield cobalt oxides that are comparatively highly active towards 4NP reduction.

The presence of induction periods, as observed herein, is common in heterogeneous catalysis, and in the context of 4NP reduction, has been attributed to a number of factors. The prevailing theories center around reconstruction of catalyst surface to yield active sites [103–106], and the time for depletion

of dissolved oxygen which competes with 4NP for  $\text{BH}_4^-$  [107–109], or as proposed more recently, could promote a rapid reversal by reacting with 4AP to regenerate 4NP [110]. However, these theories arose largely from studies of well-defined noble-metal nanoparticles, as such direct appropriation to the highly amorphous metal oxide system presented herein is not straightforward, nor is a mechanistic study of the exact surface chemistry governing the observed induction period. Nonetheless, it is evident from the structural characterization that the catalyst surfaces are coated with a number of adsorbed hydroxides and carboxyl groups (vide supra) which likely necessitates an induction period to expose or form active sites. Monitoring the pH of the reduction process at 5 min intervals reveals an initial dip upon catalyst addition (Figure S10), which could be due to the release of adsorbed species and is commensurate with the induction period timescale. Overall, pH increases as the reaction proceeds, likely due to the formation of  $\text{BO}_2^-$ .

To delineate the effects of trace KOH, a series of experiments were conducted under similar conditions. Attempted reduction of 4NP with 1 mg of KOH in lieu of Co catalyst, and in the presence of  $\text{NaBH}_4$  with monitoring at 2 min intervals for 28 min resulted in no observable decrease in 4NP\* absorbance, and no formation of 4AP\* (Figure S11A). Repeating the process in the absence of  $\text{NaBH}_4$  resulted in 4NP\* formation, and no further observable reaction over 28 min (Figure S11B). These findings are consistent with a prior report on nitrobenzene reduction [111]. Repeating the catalytic reduction of 4NP with Co@350 and the addition of 1 mg KOH facilitated reduction to 4AP\* with a  $k_{app}$  of  $0.132 \text{ min}^{-1}$  in 22 min (Figure S11C). This is only a slightly reduced rate as compared with the system without additional KOH ( $k_{app} = 0.189 \text{ min}^{-1}$ ). Yan, Xie, and coworkers have recently proposed an alternative pathway for 4NP to 4AP reduction via direct hydrogenation of 4NP to yield 4-nitrosophenol (protonated intermediate i, Figure 5), which ultimately yields 4AP/4AP\*. The presence of this species accounts for an initially enhanced absorbance at  $\lambda_{max} = 310 \text{ nm}$  [93]. We observe a similar enhanced absorbance at 310 nm which decreases as 4NP is consumed (Figure 6B and Figure S7). Thus, we postulate that increased concentration of  $\text{K}^+$  in the system, studied herein, could promote a complementary reaction pathway via 4-nitrosophenol, thus, accounting for the increased absorbance, and slight reduction in  $k_{app}$  ( $\delta = 0.057 \text{ min}^{-1}$ ) [112–115]. Overall, it is evident that trace KOH is not the driving factor in the catalytic activity reported herein but could enhance a complementary or concurrent reaction pathway, ultimately leading to the same product.

### 2.3.2. Recyclability of Co@350

Under identical conditions to our prior in situ catalysis trials with 4NP (vide supra), we tested the recyclability and long-term stability of Co@350; our most active catalyst. Prior to use, to ensure consistency throughout the recyclability trials, Co@350 was initially exposed to ambient conditions (45% to 55% RH). An immediate impact on performance, lowering the  $k_{app}$  from  $0.189 \text{ min}^{-1}$  to  $0.091 \text{ min}^{-1}$  (Table 1) was observed. This is likely due to a combination of adsorbed  $\text{H}_2\text{O}$  and  $\text{CO}_2$ , which has the dual effect of blocking sites, and lowering the catalyst weight % of the 1 mg added to the reaction mixture. Nonetheless, Co@350 remained active under medium humidity, “real-world” conditions. After every trial, the turbid solution was allowed to settle overnight, the liquid decanted, the solid washed with DIW, again decanted, and the remaining catalyst placed under vacuum overnight. The subsequent trials were conducted by the addition of 3 mL of DIW containing 4NP and  $\text{NaBH}_4$ , with monitoring at 5 min intervals. Over five trials, spanning nine days, there was an observed decrease in  $k_{app}$  of 21% (Figure 7 and Figure S12). This may be due in part to degradation of catalyst; however mechanical loss during workup is likely a significant contributor. The fluctuation in  $k_{app}$  from trial to trial is attributed to agglomeration and dispersion of particulates incurred during the workup process. Raman spectroscopy of the “spent” catalyst was indicative of predominantly  $\text{Co}_3\text{O}_4$  with characteristic peaks at 184, 460, 500, 600, and  $663 \text{ cm}^{-1}$  corresponding to the  $\text{F}_{2g}$ ,  $\text{E}_g$ ,  $\text{F}_{2g}$ ,  $\text{F}_{2g}$ , and  $\text{A}_{1g}$  modes, respectively (Figure S13) [67,68]. However, broadening of the peaks in the  $450$  to  $500 \text{ cm}^{-1}$  region, and the enhanced intensity of the signal at  $460 \text{ cm}^{-1}$  also points to the expected presence of  $\text{Co}(\text{OH})_2$  and  $\text{CoO}(\text{OH})$  [67–70]. XRD studies of spent Co@350 as well as Co@100 and Co@600 (Figure

S14) indicate the expected presence of  $\text{CoO}(\text{OH})$  and  $\text{Co}_3\text{O}_4$  for Co@350 and Co@100, and  $\text{Co}_3\text{O}_4$  for Co@600.

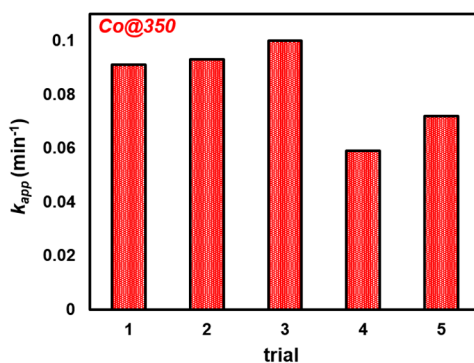


Figure 7. Recyclability of Co@350 for the reduction of 4NP\* to 4AP.

### 2.3.3. Testing Applicability of Co@350 in a Flow Process

To investigate applicability of our catalyst in a flow process [116–120], we simulated a flow reactor with a simple proof-of-concept model. Catalyst Co@350 was loaded onto two 0.22  $\mu\text{m}$  nylon syringe filters; 8 mg in filter (i) and 4 mg in filter (ii), then stacked sequentially (Figure 8A). The filters were then flushed with 10 mL of DIW to remove any loose particulates or readily dissolved species. A 60 mL syringe was loaded with 6.21  $\mu\text{mol}$  4NP, and 3.2 mmol  $\text{NaBH}_4$  in 48 mL of DIW. The syringe and filters were assembled and placed on a syringe pump, as illustrated in Figure 8A, where the solution was displaced at a rate of 0.4  $\text{mL min}^{-1}$  and the product was collected in an open flask. The bright yellow solution of 4NP\* became completely clear after passage through the filter, as confirmed by UV-Vis (Figure 8B).

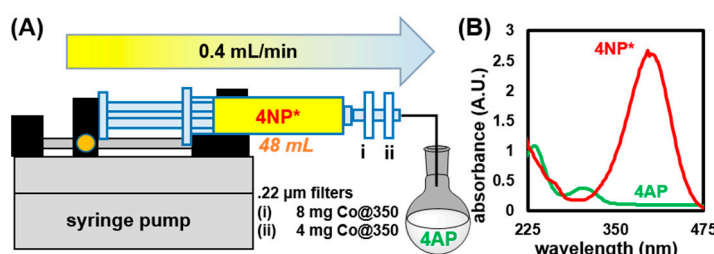
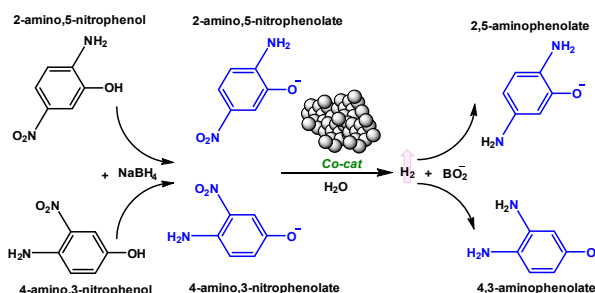


Figure 8. (A) Schematic illustration of a model flow reactor for reduction of 4NP\* to 4AP. (B) UV-Vis spectrum of 4NP\* and the resulting 4AP collected after passage through filters loaded with Co@350.

### 2.3.4. Catalytic Reduction of Amino-Nitrophenols

Encouraged by the results from the reduction of 4NP, we expanded the substrate scope to 4-amino,3-nitrophenol (4A3NP) and 2-amino,5-nitrophenol (2A5NP) (Figure 9). Therein, reactions were conducted under a similar protocol as described for 4NP. In both instances, introduction of amino-nitrophenols to a solution of  $\text{NaBH}_4$  in DIW led to a shift in absorbance commensurate with the formation of respective amino-nitrophenolates: 4-amino,3-nitrophenolate (4A3NP\*) and 2-amino,5-nitrophenolate (2A5NP\*) (Figure S4). Reactions were monitored by the disappearance of peaks at  $\lambda_{\text{max}} = 510 \text{ nm}$  (4A3NP\*) and  $\lambda_{\text{max}} = 460 \text{ nm}$  (2A5NP\*) (Figure 10, Figures S15 and S16). The recorded absorbance of the resulting diaminophenolates, 4,3-aminophenolate (4A3NP\*) and 2,5-aminophenolate (25AP\*), were consistent with prior literature [121–124].



**Figure 9.** Reaction process of amino-nitrophenols with catalysts Co@100, Co@350 and Co@600 (“Co-cat”) in H<sub>2</sub>O with excess NaBH<sub>4</sub>.

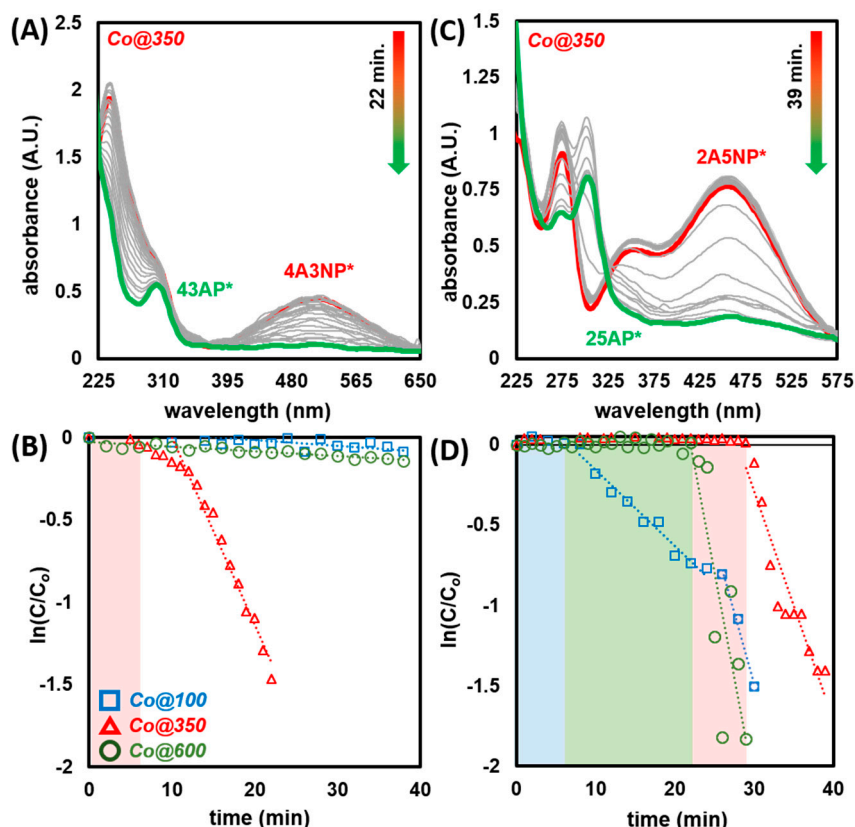


**Figure 10.** (A) UV-Vis spectra of the reduction of 4A3NP by Co@350 (SI for Co@100 and Co@600) and (B) plot of  $\ln(C/C_0)$  as a function of time for the reduction of 4A3NP by Co@100, Co@350, and Co@600. (C) UV-Vis spectra of the reduction of 2A5NP by Co@350 (SI for Co@100 and Co@600) and (D) plot of  $\ln(C/C_0)$  as a function of time for the reduction of 2A5NP by Co@100, Co@350, and Co@600. Note, color blocks represent induction times.

In the case of 4A3NP, the results from the initial 4NP trials were accurately predictive. Within the tested time of 40 min, Co@350 rapidly facilitated reduction ( $k_{app} = 0.114 \text{ min}^{-1}$ ), whereas both Co@100 and Co@600 displayed only negligible activity ( $k_{app} = 0.004$  and  $0.003 \text{ min}^{-1}$  respectively). By switching the position of the amine and nitro groups to 2A5NP, activity across all three catalysts changed dramatically (Figure 10 and Table 1). Co@100 appeared to exhibit two distinctly different rates; after an induction time of 8 min, reduction proceeded at a modest rate ( $k_{app} = 0.047 \text{ min}^{-1}$ ), this increased sharply at ca. 26 min to  $0.175 \text{ min}^{-1}$ . We tentatively attribute this to the multi-component nature of Co@100, wherein initial activity may be due to Co(OH)<sub>2</sub> species, and the increased, latent rate to CoO(OH) or Co<sub>3</sub>O<sub>4</sub> as available in the other catalysts. This is commensurate with both the rates and induction times observed for Co@350 and Co@600 (vide supra). The highest rate observed was for Co@600 ( $k_{app} = 0.264 \text{ min}^{-1}$ ) with an induction time of 22 min. The slowest catalyst

was Co@350, exhibiting both the lowest rate ( $k_{app} = 0.143 \text{ min}^{-1}$ ) and longest induction (28 min). In this case, the observed rates for Co@350 and Co@600 inversely correlate to BET surface area (Co@350 =  $28.28 \text{ m}^2 \text{ g}^{-1}$ , Co@600 =  $10.38 \text{ m}^2 \text{ g}^{-1}$ ). The difference in reactivity is, therefore, more likely related to the nature of available surface sites as dictated by the particle size, degree of crystallinity (vide supra), and the combination of CoO(OH) and Co<sub>3</sub>O<sub>4</sub> available. These findings highlight the potential of fine-tuning activity and selectivity for cobalt oxide- and hydroxide-based catalysts through combined mechanochemical synthesis and thermal treatment. Furthermore, they call in to question the common practice of comparing the activity of heterogeneous catalysts based on 4NP screening alone. As noted herein, addition and respective position of functional groups to the 4NP scaffold can easily reverse observed rates from the ubiquitous 4NP model reaction [125].

### 3. Materials and Methods

All reactions were carried out under ambient (21 to 23 °C, 45% to 55% relative humidity). Cobalt(II) chloride hexahydrate, 4-nitrophenol (4NP), 4-amino,3-nitrophenol (4A3NP), 2-amino,5-nitrophenol (2A5NP), anilines, and NaBH<sub>4</sub> were purchased from TCI America, KOH was purchased from Strem Chemicals, and used as received. Co<sub>3</sub>O<sub>4</sub> (99.7%) was purchased from Alfa Aesar and used as received. FTIR Spectra were measured on a Bruker Vertex-70 with Helios ATR attachment. UV-Vis Spectra were collected on an Agilent Cary 60 spectrophotometer utilizing 1 cm quartz cuvettes. Optical microscope images were collected on a Leica DM2500m with an Accu-Scope Excelis-HD camera. The pH measurements were conducted with an Ohaus 2100 m with ST210 electrode. Pressure change due to H<sub>2</sub> evolution was measured in a closed system with a Vernier PS400-BTA sensor. The N<sub>2</sub> gas adsorption isotherm analysis was performed using a Micromeritics ASAP 2020 surface area and porosity analyzer. Measurements were performed at 77 K (liquid N<sub>2</sub> bath) on thermally activated samples. The BET surface areas were obtained by performing a Rouquerol analysis over the linear isotherm to determine the upper limits of the BET model. Least squares linear fitting over the BET plot provided the parameter for the volume of the monolayer, surface area, and C-constant, following the recommendation by Rouquerol [80]. The powder X-ray diffraction measurements were performed using a Rigaku Miniflex 600 diffractometer, with 2 $\theta$  Bragg-Brentano geometry, a 300 mm goniometer diameter, and a 600 W (40 kV, 15 mA) X-ray tube source using Ni-filtered CuK $\alpha$  ( $\lambda = 1.5418 \text{ \AA}$ ) radiation, equipped with a high-resolution D/tex 250 detector, 5.0° incident and receiving Soller slits, a 0.625° divergent slit, a 1.25° scattering slit, a 0.3 mm receiving slit, a Ni-CuK $\beta$  filter, and an anti-scattering blade. Samples were measured from 10 to 55 2-theta degrees with a step size of 0.02 degrees and a scan rate of 0.5 min per step. Powder samples were prepared by depositing the powder sample on a silicon zero-background sample holder and gently pressing the powder with a glass slide. Raman data were acquired using a Horiba XploRA-plus microscope with a 785 nm laser excitation source. The laser was focused onto the samples using 100 $\times$  objective producing a spot size of  $\sim 1 \mu\text{m}$ . Spectra were acquired from 20 to 2000  $\text{cm}^{-1}$  with 10 s acquisition time. The SEM images were acquired with a LEO 1450VP and accompanied by an Oxford EDX for elemental analysis. All samples were mounted on metal and silver-coated to provide enhanced contrast images. Bright field (BF) images were obtained with the help FEI Tecnai F 30 TEM in conventional transmission electron microscopy (CTEM) mode at an operating voltage of 300 kV. The X-ray photoelectron spectra (XPS) were obtained using a Thermo Scientific ESCALAB XI+ X-ray Photoelectron Spectrometer with an Al K $\alpha$  X-ray source (1486.67 eV). The TEM samples were prepared by prolonged sonication of samples in methanol at 40 °C followed by dispersion on CF-2/4-3Cu-25 C-flat<sup>TM</sup> holey carbon on copper grids from Electron Microscopy Sciences.

### 4. Conclusions

Reduction of nitrophenols is typically carried out by either noble-metal nanoparticles, or alternatives synthesized with precise control over size and shape. This requires a significant expenditure of either material cost, experimental effort, or in many cases, both. These factors can present an obstacle to any practical, large-scale application as would be necessitated for environmental

remediation. The process reported, herein, represents a facile route to bulk cobalt-oxide based materials, via a combined mechanochemical (vibratory ball milling) and calcination approach. By utilizing inexpensive starting materials such as  $\text{CoCl}_2(\text{H}_2\text{O})_6$  and KOH, no solvent during synthesis, and only DIW for workup, it remains both economical and sustainable. Calcination at 100, 350, and 600 °C afforded three materials (Co@100, Co@350 and Co@600) composed of increasing amounts of  $\text{Co}_3\text{O}_4$  and decreasing amounts of  $\text{CoO}(\text{OH})$ . All materials can generally be described as micron-sized compacted agglomerates of nanoplates. All three were active for the reduction of 4NP, with activity varying based on a combination of chemical composition, crystallinity, and surface area. Therein, Co@350 displayed the best performance and was further studied for recyclability and applicability in a flow process, where it was shown to remain active after prolonged exposure to air and moisture.

Expanding the substrate scope to amine-functionalized nitrophenols revealed unexpected results. While 4A3NP reflected the trends observed with the 4NP model system, 2A5NP presented a complete reversal, where Co@100 was overall the more active species. This brings to light several interesting points. First, by combining the mechanochemical method and varying subsequent calcination temperatures, different mixtures of cobalt oxides and hydroxides can be achieved, the consequence of which dramatically alters both activity and selectivity. Second, it serves caution not to dismiss potential catalysts which underperform with the now ubiquitous 4NP model, and therefore could display enhanced reactivity with other functionalities. Our ongoing efforts focus on understanding the influence of cobalt oxide and hydroxide mixtures which govern the observed reactivity and selectivity with the aim of developing a precise mechanism for NP reduction by early transition-metal oxides.

**Supplementary Materials:** The supplementary materials are available online.

**Author Contributions:** Conceptualization, T.J. and L.R.S.; methodology, L.R.S., T.J., M.B., F.J.U.-R.; analysis, L.R.S., B.M., M.B., K.O.D., H.A., W.J.N.; synthesis, T.E.S.; writing—original draft preparation and review and editing, M.B., F.J.U.-R., T.J.; supervision, T.J., M.B., F.J.U.-R. All authors have read and agreed to the published version of the manuscript.

**Funding:** This work was supported by start-up funding from the Department of Chemistry, College of Science, the FCI at the University of Central Florida, and partially by NSF CHE-1665277.

**Acknowledgments:** We thank W.E.K., UCF Physics, for access to a SPEX 8000 mill, and T.C., UCF Chemistry for calcination experiments, and P.B., UCF MSE for helpful discussion. Authors acknowledge the NSF MRI: XPS: ECCS: 1726636, hosted in MCF-AMPAC facility, MSE, CECS. L.R.S. and B.M. contributed equally. L.R.S. thanks the UCF Office of Undergraduate Research for a Student Research Grant Award.

**Conflicts of Interest:** The authors declare no conflicts of interest.

## References

1. Yi, S.; Zhuang, W.-Q.; Wu, B.; Tiong-Lee, S.; Tay, J.-H. Biodegradation of p-nitrophenol by aerobic granules in a sequencing batch reactor. *Environ. Sci. Technol.* **2006**, *40*, 2396–2401. [[CrossRef](#)] [[PubMed](#)]
2. Podeh, M.R.H.; Bhattacharya, S.K.; Qu, M. Effects of nitrophenol on acetate utilizing methanogenic systems. *Wat. Res.* **1995**, *29*, 391–399. [[CrossRef](#)]
3. Xia, J.; He, G.; Zhang, L.; Sun, X.; Wang, X. Hydrogenation of nitrophenols catalyzed by carbon black-supported nickel nanoparticles under mild conditions. *Appl. Catal. B* **2016**, *180*, 408–415. [[CrossRef](#)]
4. Yu, S.; Hu, J.; Wang, J. Gamma radiation-induced degradation of p-nitrophenol (PNP) in the presence of hydrogen peroxide ( $\text{H}_2\text{O}_2$ ) in aqueous solution. *J. Hazard. Mater.* **2010**, *177*, 1061–1067. [[CrossRef](#)] [[PubMed](#)]
5. Ju, K.-S.; Parales, R.E. Nitroaromatic compounds, from synthesis to biodegradation. *Microbiol. Mol. Biol. Rev.* **2010**, *74*, 250–272. [[CrossRef](#)]
6. Zhao, H.; Kong, C.-H. Enhanced removal of p-nitrophenol in a microbial fuel cell after a long-term operation and the catabolic versatility of its microbial community. *Chem. Eng. J.* **2018**, *339*, 424–431. [[CrossRef](#)]
7. Sun, M.; Reible, D.D.; Lowry, G.V.; Gregory, K.B. Effect of applied voltage, initial concentration, and natural organic matter on sequential reduction/oxidation of nitrobenzene by graphite electrodes. *Environ. Sci. Technol.* **2012**, *46*, 6174–6181. [[CrossRef](#)]
8. Downing, R.S.; Kunkeler, P.J.; van Bekkum, H. Catalytic synthesis of aromatic amines. *Catal. Today* **1997**, *37*, 121–136. [[CrossRef](#)]

9. Wegener, G.; Brandt, M.; Duda, L.; Hofmann, J.; Kleszczewski, B.; Koch, D.; Kumpf, R.-J.; Orzesek, H.; Pirkl, H.-G.; Six, C.; et al. Trends in industrial catalysis in the polyurethane industry. *Appl. Catal. A* **2001**, *22*, 303–335. [[CrossRef](#)]
10. Nomura, K. Transition metal catalyzed hydrogenation of reduction in water. *J. Mol. Catal. A* **1998**, *130*, 1–28. [[CrossRef](#)]
11. Espinosa Bosch, M.; Ruiz Sánchez, A.J.; Sánchez Rojas, F.; Bosh Ojeda, C. Determination of paracetamol: Historical evolution. *J. Pharm. Biomed. Anal.* **2006**, *42*, 291–321. [[CrossRef](#)] [[PubMed](#)]
12. Xiong, Z.; Zhang, H.; Zhang, W.; Lai, B.; Yao, G. Removal of nitrophenols and their derivatives by chemical redox: A review. *Chem. Eng. J.* **2019**, *359*, 13–31. [[CrossRef](#)]
13. Aditya, T.; Pal, A.; Pal, T. Nitroarene reduction: A trusted model reaction to test nanoparticle catalysts. *Chem. Commun.* **2015**, *51*, 9410–9431. [[CrossRef](#)] [[PubMed](#)]
14. Zhao, P.; Feng, X.; Huang, D.; Yang, G.; Astruc, D. Basic concepts and recent advances in nitrophenol reduction by gold- and other transition metal nanoparticles. *Coord. Chem. Rev.* **2015**, *287*, 114–136. [[CrossRef](#)]
15. Hervés, P.; Pérez-Lorenzo, M.; Liz-Marzán, L.M.; Dzubielia, J.; Lu, Y.; Ballauff, M. Catalysis by metallic nanoparticles in aqueous solution: Model reactions. *Chem. Soc. Rev.* **2012**, *41*, 5577–5587. [[CrossRef](#)]
16. Menumerov, E.; Hughes, R.A.; Golze, S.D.; Neal, R.D.; Demille, T.B.; Campanaro, J.C.; Kotesky, K.C.; Rouvimov, S.; Neretiva, S. Identifying the true catalyst in the reduction of 4-nitrophenol: A case study showing the effect of leaching and oxidative etching using Ag catalysts. *ACS Catal.* **2018**, *8*, 8879–8888. [[CrossRef](#)]
17. Menumerov, E.; Hughes, R.A.; Neretina, S. One-step catalytic reduction of 4-nitrophenol through the direct injection of metal salts into oxygen-depleted reactants. *Catal. Sci. Technol.* **2017**, *7*, 1460–1464. [[CrossRef](#)]
18. Dolatkhah, A.; Jani, P.; Wilson, L.D. Redox-responsive polymer template as an advanced multifunctional catalyst support for silver nanoparticles. *Langmuir* **2018**, *34*, 10560–10568. [[CrossRef](#)]
19. Hsia, C.-F.; Madasu, M.; Huang, M. Aqueous phase synthesis of Au-Cu core-shell nanocubes and octahedra with tunable sizes and noncentrally located cores. *Chem. Mater.* **2016**, *28*, 3073–3079. [[CrossRef](#)]
20. Bari, N.K.; Kumar, G.; Bhatt, A.; Hazra, J.P.; Garg, A.; Ali, M.E.; Sinha, S. Nanoparticle fabrication on bacterial microcompartment surface for the development of hybrid enzyme-inorganic catalyst. *ACS Catal.* **2018**, *8*, 7742–7748. [[CrossRef](#)]
21. Wang, F.; Li, W.; Feng, X.; Liu, D.; Zhang, Y. Decoration of Pt on Cu/Co double-doped CeO<sub>2</sub> nanospheres and their greatly enhanced catalytic activity. *Chem. Sci.* **2016**, *7*, 1867–1873. [[CrossRef](#)] [[PubMed](#)]
22. Johnson, J.A.; Makis, J.J.; Marvin, K.A.; Rodenbusch, S.E.; Stevenson, K.J. Size-dependant hydrogenation of p-nitrophenol with Pd nanoparticles synthesized with poly(amido)amine dendrimer templates. *J. Phys. Chem. C* **2013**, *117*, 22644–22651. [[CrossRef](#)]
23. Jadbabaei, N.; Slobodjian, R.J.; Shuai, D.; Zhang, H. Catalytic reduction of 4-nitrophenol by palladium-resin composites. *Appl. Catal.* **2017**, *543*, 209–217. [[CrossRef](#)]
24. Islam, M.T.; Saenz-Arana, R.; Wang, H.; Bernal, R.; Noveron, J.C. Green synthesis of gold, silver, platinum, and palladium nanoparticles reduced and stabilized by sodium rhodizonate and their catalytic reduction of 4-nitrophenol and methyl orange. *New J. Chem.* **2018**, *42*, 6472–6478. [[CrossRef](#)]
25. Liu, A.; Traulsen, C.H.-H.; Cornelissen, J.J.L.M. Immobilization of catalytic virus-like particles in a flow reactor. *Chem. Commun.* **2017**, *53*, 7632–7634. [[CrossRef](#)]
26. Koklioti, M.A.; Skaltsas, T.; Sato, Y.; Suenaga, K.; Stergiou, A.; Tagmatarchis, N. Mechanistic insights into the photocatalytic properties of metal nanocluster/graphene ensembles. Examining the role of visible light in the reduction of 4-nitrophenol. *Nanoscale* **2017**, *9*, 9685–9692. [[CrossRef](#)]
27. Bingwa, N.; Meijboom, R. Kinetic evaluation of dendrimer-encapsulated palladium nanoparticles in the 4-nitrophenol reduction reaction. *J. Phys. Chem. C* **2014**, *118*, 19849–19858. [[CrossRef](#)]
28. Islam, M.T.; Jing, H.; Yang, T.; Zubia, E.; Goos, A.G.; Bernal, R.A.; Botez, C.E.; Narayan, M.; Chan, C.K.; Noveron, J.C. Fullerene stabilized gold nanoparticles supported on titanium dioxide for enhanced photocatalytic degradation of methyl orange and catalytic reduction of 4-nitrophenol. *J. Environ. Chem. Eng.* **2018**, *6*, 3827–3836. [[CrossRef](#)]
29. Nguyen, T.B.; Huang, C.P.; Doong, R.-A. Enhanced catalytic reduction of nitrophenols by sodium borohydride over highly recyclable Au@graphitic carbon nitride nanocomposites. *Appl. Catal. B* **2019**, *240*, 337–347. [[CrossRef](#)]

30. Wu, Y.; Wen, M.; Wu, Q.-S.; Fang, H. Ni/graphene nanostructure and its electron-enhanced catalytic action for hydrogenation reaction of nitrophenol. *J. Phys. Chem. C* **2014**, *118*, 6307–6313. [[CrossRef](#)]
31. Wang, X.; Lu, J.; Zhao, Y.; Wang, X.; Lin, Z.; Liu, X.; Wu, R.; Yang, C.; Su, X. Facile fabrication of nickel/heazlewoodite@carbon nanosheets and their superior catalytic performance of 4-nitrophenol reduction. *ChemCatChem* **2018**, *10*, 4143–4153. [[CrossRef](#)]
32. Mandlimath, T.R.; Gopal, B. Catalytic activity of first row transition metal oxides in the conversion of p-nitrophenol to p-aminophenol. *J. Mol. Catal. A* **2011**, *350*, 9–15. [[CrossRef](#)]
33. Mohamed, M.J.S.; Denthaje, K.B. Novel RGO-ZnWO<sub>4</sub>-Fe<sub>3</sub>O<sub>4</sub> nanocomposites as an efficient catalyst for rapid reduction of 4-nitrophenol to 4-aminophenol. *Ind. Eng. Chem. Res.* **2016**, *55*, 7267–7272. [[CrossRef](#)]
34. Qiao, X.-Q.; Zhang, Z.-W.; Hou, D.-F.; Li, D.-S.; Liu, Y.; Lan, Y.-Q.; Zhang, J.; Feng, P.; Bu, X. Tunable MoS<sub>2</sub>/SnO<sub>2</sub> P-N heterojunctions for an efficient trimethylamine gas sensor and 4-nitrophenol reduction catalyst. *ACS Sustain. Chem. Eng.* **2018**, *6*, 12375–12384. [[CrossRef](#)]
35. Ma, Y.; Ni, Y.; Guo, F.; Xiang, N. Flowerlike copper(II)-based coordination polymers particles: Rapid room-temperature fabrication, influencing factors, and transformation toward CuO microstructures with good catalytic activity for the reduction of 4-nitrophenol. *Cryst. Growth Des.* **2015**, *15*, 2243–2252. [[CrossRef](#)]
36. Shtansky, D.V.; Firestein, K.L.; Goldberg, D.V. Fabrication and application of BN nanoparticles, nanosheets and their nanohybrids. *Nanoscale* **2018**, *10*, 17477–17493. [[CrossRef](#)]
37. Huang, C.; Ye, W.; Liu, Q.; Qiu, X. Dispersed Cu<sub>2</sub>O octahedrons on h-BN nanosheets for p-nitrophenol reduction. *ACS Appl. Mater. Interfaces* **2014**, *6*, 14469–14476. [[CrossRef](#)]
38. Zhang, K.; Liu, Y.; Deng, J.; Xie, S.; Lin, H.; Zhao, X.; Yang, J.; Han, Z.; Dai, H. Fe<sub>2</sub>O<sub>3</sub>/3DOM BiVO<sub>4</sub>: High-performance photocatalysts for the visible light-driven degradation of 4-nitrophenol. *Appl. Catal. B* **2017**, *202*, 569–579. [[CrossRef](#)]
39. Kong, X.-K.; Sun, Z.-Y.; Chen, M.; Chen, C.; Chen, Q. Metal-free catalytic reduction of 4-nitrophenol to 4-aminophenol by N-doped grapheme. *Energy Environ. Sci.* **2013**, *6*, 3260–3266. [[CrossRef](#)]
40. Gao, L.; Li, R.; Sui, X.; Li, R.; Chen, C.; Chen, Q. Conversion of chicken feather waste to N-doped carbon nanotubes for the catalytic reduction of 4-nitrophenol. *Environ. Sci. Technol.* **2014**, *48*, 10191–10197. [[CrossRef](#)]
41. Wu, Q.; Liang, M.; Zhang, S.; Liu, X.; Wang, F. Development of function black phosphorus nanosheets with remarkable catalytic and antibacterial performance. *Nanoscale* **2018**, *10*, 10428–10435. [[CrossRef](#)] [[PubMed](#)]
42. Raza, W.; Krupanidhi, S.B. Engineering defects in graphene oxide for selective ammonia and enzyme-free glucose sensing and excellent catalytic performance for para-nitrophenol reduction. *ACS Appl. Mater. Interfaces* **2018**, *10*, 25285–25294. [[CrossRef](#)] [[PubMed](#)]
43. Zhang, J.; Zhang, F.; Yang, Y.; Guo, S.; Zhang, J. Composites of graphene quantum dots and reduced graphene oxide as catalysts for nitroarene reduction. *ACS Omega* **2017**, *2*, 7293–7298. [[CrossRef](#)] [[PubMed](#)]
44. Stergiou, A.; Tagmatarchis, N. Fluorene-perylene diimide arrays onto graphene sheets for photocatalysis. *ACS Appl. Mater. Interfaces* **2016**, *8*, 21576–21584. [[CrossRef](#)] [[PubMed](#)]
45. Han, Q.; Chen, N.; Zhang, J.; Qu, L. Graphene/graphitic carbon nitride hybrids for catalysis. *Mater. Horiz.* **2017**, *4*, 832–850. [[CrossRef](#)]
46. Wang, Z.; Su, R.; Wang, D.; Shi, J.; Wang, J.-X.; Pu, Y.; Chen, J.-F. Sulfurized graphene as efficient metal-free catalysts for reduction of 4-nitrophenol to 4-aminophenol. *Ind. Eng. Chem. Res.* **2017**, *56*, 13610–13617. [[CrossRef](#)]
47. Pan, L.; Tang, J.; Wang, F. Synthesis and electrocatalytic performance for p-nitrophenol reduction of rod-like Co<sub>3</sub>O<sub>4</sub> and Ag/Co<sub>3</sub>O<sub>4</sub> composites. *Mater. Res. Bull.* **2013**, *48*, 2648–2653. [[CrossRef](#)]
48. Mogudi, B.M.; Ncube, P.; Meijboom, R. Catalytic activity of mesoporous cobalt oxides with controlled porosity and crystallite sizes: Evaluation using the reduction of 4-nitrophenol. *Appl. Catal. B* **2016**, *74*, 74–82. [[CrossRef](#)]
49. Mogudi, B.M.; Ncube, P.; Bingwa, N.; Mawila, N.; Mathebula, S.; Meijboom, R. Promotion effects of alkali- and alkaline earth metals on catalytic activity of mesoporous Co<sub>3</sub>O<sub>4</sub> for 4-nitrophenol reduction. *Appl. Catal. B* **2017**, *218*, 240–248. [[CrossRef](#)]
50. Chen, H.; Yang, M.; Tao, S.; Chen, G. Oxygen vacancy enhanced catalytic activity of reduced Co<sub>3</sub>O<sub>4</sub> towards p-nitrophenol reduction. *Appl. Catal. B* **2017**, *209*, 648–656. [[CrossRef](#)]
51. Song, T.; Ren, P.; Duan, Y.; Wang, Z.; Chen, X.; Yang, Y. Cobalt nanocomposites on N-doped hierarchical porous carbon for highly selective formation of anilines and imines from nitroarenes. *Green Chem.* **2018**, *20*, 4629–4637. [[CrossRef](#)]

52. Chinnappan, A.; Eshkalak, S.K.; Baskar, C.; Khatibzadeh, M.; Kowsari, E.; Ramakrishna, S. Flower-like 3-dimensional hierarchical  $\text{Co}_3\text{O}_4/\text{NiO}$  microspheres for 4-nitrophenol reduction reaction. *Nanoscale Adv.* **2019**, *1*, 305–313. [[CrossRef](#)]
53. Park, J.-W.; Park, C.-M. Mechanochemically induced transformation of  $\text{CoO}(\text{OH})$  into  $\text{Co}_3\text{O}_4$  nanoparticles and their highly reversible Li storage characteristics. *RSC Adv.* **2017**, *7*, 10618–10623. [[CrossRef](#)]
54. Shaw, T.E.; Shultz, L.R.; Garayeva, L.R.; Blair, R.G.; Noll, B.C.; Jurca, T. Mechanochemical routes for the synthesis of acetyl- and bis-(imino)pyridine ligands and organometallics. *Dalton Trans.* **2018**, *47*, 16876–16884. [[CrossRef](#)]
55. He, G.; Ding, J.; Zhang, J.; Hao, Q.; Chen, H. One-step ball-milling preparation of highly photocatalytic active  $\text{CoFe}_2\text{O}_4$ -reduced graphene oxide heterojunctions for organic dye removal. *Ind. Eng. Chem. Res.* **2015**, *54*, 2862–2867. [[CrossRef](#)]
56. Lyu, H.; Gao, B.; He, F.; Ding, C.; Tang, J.; Crittenden, J.C. Ball-milled carbon nanomaterials for energy and environmental applications. *ACS Sustain. Chem. Eng.* **2017**, *5*, 9568–9585. [[CrossRef](#)]
57. Peters, D.W.; Blair, R.G. Mechanochemical synthesis of an organometallic compound: A high volume manufacturing method. *Faraday Discuss.* **2014**, *170*, 83–91. [[CrossRef](#)]
58. Restrepo, D.; Hick, S.M.; Griebel, C.; Alarcón, J.; Giesler, K.; Chen, Y.; Orlovskaya, N.; Blair, R.G. Size controlled mechanochemical synthesis of  $\text{ZrSi}_2$ . *Chem. Commun.* **2013**, *49*, 707–709. [[CrossRef](#)]
59. Zhao, B.; Zheng, Y.; Ye, F.; Deng, X.; Xu, X.; Liu, M.; Shao, Z. Multifunctional iron oxide nanoflake/graphene composites derived from mechanochemical synthesis for enhanced lithium storage and electrocatalysis. *ACS Appl. Mater. Interfaces* **2015**, *7*, 14446–14455. [[CrossRef](#)]
60. Muñoz-Batista, M.J.; Rodríguez-Padron, D.; Puente-Santiago, A.R.; Luque, R. Mechanochemistry: Toward sustainable design of advanced nanomaterials for electrochemical energy storage and catalytic applications. *ACS Sustain. Chem. Eng.* **2018**, *6*, 9530–9544. [[CrossRef](#)]
61. Saitow, K.; Wang, Y.; Takahashi, S. Mechano-synthesized orange  $\text{TiO}_2$  shows significant photocatalysis under visible light. *Sci. Rep.* **2018**, *8*, 15549. [[CrossRef](#)] [[PubMed](#)]
62. Jeon, I.-Y.; Choi, H.-J.; Choi, M.; Seo, J.-M.; Jung, S.-M.; Kim, M.-J.; Zhang, S.; Zhang, L.; Xia, Z.; Dai, L.; et al. Facile, scalable synthesis of edge-halogenated graphene nanoplatelets as efficient metal-free electrocatalysis for oxygen reduction reaction. *Sci. Rep.* **2013**, *3*, 1810. [[CrossRef](#)] [[PubMed](#)]
63. Prochowicz, D.; Nawrocki, J.; Terlecki, M.; Marynowski, W.; Lewiński, J. Facile mechanosynthesis of the archetypal Zn-based metal-organic frameworks. *Inorg. Chem.* **2018**, *57*, 13437–13442. [[CrossRef](#)] [[PubMed](#)]
64. Yang, J.; Liu, H.; Martens, W.N.; Frost, R.L. Synthesis and characterization of cobalt hydroxide, cobalt oxyhydroxide, and cobalt oxide nanodiscs. *J. Phys. Chem. C* **2010**, *114*, 111–119. [[CrossRef](#)]
65. Solsona, B.; Davies, T.E.; Garcia, T.; Vásquez, I.; Dejoz, A.; Taylor, S.H. Total oxidation of propane using nanocrystalline cobalt oxide and supported cobalt oxide catalysts. *Appl. Catal. B* **2008**, *84*, 176–184. [[CrossRef](#)]
66. Liu, F.; Su, H.; Jin, L.; Zhang, H.; Chu, X.; Yang, W. Facile synthesis of ultrafine cobalt oxide nanoparticles for high-performance supercapacitors. *J. Colloid Interface Sci.* **2017**, *505*, 796–804. [[CrossRef](#)] [[PubMed](#)]
67. Nguyen, T.; Boudard, M.; Rapenne, L.; Chaix-Pluchery, O.; Carmezim, M.J.; Montemor, M.F. Structural evolution, magnetic properties and electrochemical response of  $\text{MnCo}_2\text{O}_4$  nanosheet films. *RSC Adv.* **2015**, *5*, 27844–27852. [[CrossRef](#)]
68. Hadjiev, V.G.; Iliev, M.N.; Vergilov, I.V. The Raman spectra of  $\text{Co}_3\text{O}_4$ . *J. Phys. C Solid State Phys* **1988**, *21*, L199–L201. [[CrossRef](#)]
69. Liu, Y.-C.; Koza, J.A.; Switzer, J.A. Conversion of electrodeposited  $\text{Co}(\text{OH})_2$  to  $\text{CoOOH}$  and  $\text{Co}_3\text{O}_4$ , and comparison of their catalytic activity for the oxygen evolution reaction. *Electrochim. Acta* **2014**, *140*, 359–365. [[CrossRef](#)]
70. Alrehaily, L.M.; Joseph, J.M.; Wren, J.C. Radiation-induced formation of  $\text{Co}_3\text{O}_4$  nanoparticles from  $\text{Co}^{2+}(\text{aq})$ : Probing the kinetics using radical scavengers. *Phys. Chem. Chem. Phys.* **2015**, *17*, 24138–24150. [[CrossRef](#)]
71. Zhang, J.; Gao, W.; Dou, M.; Wang, F.; Liu, J.; Li, Z.; Li, J. Nanorod-constructed porous  $\text{Co}_3\text{O}_4$  nanowires: Highly sensitive sensors for the detection of hydrazine. *Analyst* **2015**, *140*, 1686–1692. [[CrossRef](#)]
72. Pandey, B.K.; Shahi, A.K.; Gopal, R. Magnetic colloid by PLA: Optical, magnetic and thermal transport properties. *Appl. Surf. Sci.* **2015**, *347*, 461–470. [[CrossRef](#)]
73. Li, N.; Zhu, Y.D.; Liu, T.; Liu, S.G.; Lin, S.M.; Shi, Y.; Luo, H.Q.; Li, N.B. Turn-on fluorescence detection of pyrophosphate anion based on DNA-attached cobalt oxyhydroxide. *New J. Chem.* **2017**, *41*, 1993–1996. [[CrossRef](#)]

74. Nie, Q.; Cai, Q.; Xu, H.; Qiao, Z.; Li, Z. A facile colorimetric method for highly sensitive ascorbic acid detection by using CoOOH nanosheets. *Anal. Methods* **2018**, *10*, 2623–2628. [[CrossRef](#)]
75. Mahmoud, W.E.; Al-Agel, F.A. A novel strategy to synthesize cobalt hydroxide and Co<sub>3</sub>O<sub>4</sub> nanowires. *J. Phys. Chem. Solids* **2011**, *72*, 904–907. [[CrossRef](#)]
76. Alburquenque, D.; Vargas, E.; Denardin, J.C.; Escrig, J.; Marco, J.F.; Ortiz, J.; Gautier, J.L. Physical and electrochemical study of cobalt oxide nano- and microparticles. *Mater. Charact.* **2014**, *93*, 191–197. [[CrossRef](#)]
77. He, T.; Chen, D.R.; Jiao, X.L.; Wang, Y.L. Co<sub>3</sub>O<sub>4</sub> nanoboxes: Surfactant-templated fabrication and microstructure characterization. *Adv. Mater.* **2006**, *18*, 1078–1082. [[CrossRef](#)]
78. Taibi, M.; Ammar, S.; Jouini, N.; Fiévet, F.; Molinié, P.; Drillon, M. Layered nickel hydroxide salt: Synthesis, characterization and magnetic behaviour in relation to the basal spacing. *J. Mater. Chem.* **2002**, *12*, 3238–3244. [[CrossRef](#)]
79. Wang, L.; Lin, C.; Zhang, F.; Jin, J. Phase transformation guided single-layer β-Co(OH)<sub>2</sub> nanosheets for pseudocapacitive electrodes. *ACS Nano*. **2014**, *8*, 3724–3734. [[CrossRef](#)] [[PubMed](#)]
80. George, G.; Anandhan, S. A comparative study on physico-chemical properties of sol-gel electrospun cobalt oxide nanofibers from two different polymeric binders. *RSC Adv.* **2015**, *5*, 81429–81437. [[CrossRef](#)]
81. Roquerol, F.; Roquerol, J.; Sing, K. *Adsorption by Powders and Porous Solids: Principles, Methodology and Applications*; Academic Press: San Diego, CA, USA, 1999.
82. Moulder, J.F.; Stickle, W.F.; Sobol, P.E.; Bomben, K.D. *Handbook of X-ray Photoelectron Spectroscopy*; Physical Electronics Press: Eden Prairie, MN, USA, 1995.
83. Rodella, C.B.; Barrett, D.H.; Moya, S.F.; Figueroa, S.J.A.; Pimenta, M.T.B.; Curvelo, A.A.S.; Silva, V.T.D. Physical and Chemical Studies of Tungsten Carbide Catalysts: Effects of Ni Promotion and Sulphonated Carbon. *RSC Adv.* **2015**, *30*, 23874–23885. [[CrossRef](#)]
84. Nguyen-Huy, C.; Lee, J.; Seo, J.H.; Yang, E.; Lee, J.; Choi, K.; Lee, H.; Kim, J.H.; Lee, M.S.; Joo, S.H.; et al. An Structure-Dependent Catalytic Properties of Mesoporous Cobalt Oxides in Furfural Hydrogenation. *Appl. Catal. A Gen.* **2019**, *583*, 117125. [[CrossRef](#)]
85. Li, Y.; Tan, B.; Wu, Y. Mesoporous Co<sub>3</sub>O<sub>4</sub> Nanowire Arrays for Lithium Ion Batteries with High Capacity and Rate Capability. *Nano Lett.* **2008**, *8*, 265–270. [[CrossRef](#)] [[PubMed](#)]
86. Damjanović, L.; Majchrzak, M.; Bennici, S.; Auroux, A. Determination of the heat evolved during sodium borohydride hydrolysis catalyzed by Co<sub>3</sub>O<sub>4</sub>. *Int. J. Hydrog. Energy* **2011**, *36*, 1991–1997. [[CrossRef](#)]
87. Wei, L.; Dong, X.; Ma, M.; Lu, Y.; Wang, D.; Zhang, S.; Zhao, D.; Wang, Q. Co<sub>3</sub>O<sub>4</sub> hollow fiber: An efficient catalyst precursor for hydrolysis of sodium borohydride to generate hydrogen. *Int. J. Hydrog. Energy* **2018**, *43*, 1529–1533. [[CrossRef](#)]
88. Demirci, U.B.; Miele, P. Cobalt in NaBH<sub>4</sub> hydrolysis, *Phys. Chem. Chem. Phys.* **2012**, *12*, 14651–14665. [[CrossRef](#)]
89. Antonels, N.C.; Meijboom, R. Preparation of well-defined dendrimer encapsulated ruthenium nanoparticles and their evaluation in the reduction of 4-nitrophenol according to the Langmuir-Hinshelwood approach. *Langmuir* **2013**, *29*, 13433–13442. [[CrossRef](#)]
90. Wunder, S.; Lu, Y.; Albrecht, M.; Ballauf, M. Catalytic activity of faceted gold nanoparticles studied by a model reaction: Evidence for substrate-induced surface restructuring. *ACS Catal.* **2011**, *1*, 908–916. [[CrossRef](#)]
91. Wunder, S.; Polzer, F.; Lu, Y.; Mei, Y.; Ballauf, M. Kinetic analysis of catalytic reduction of 4-nitrophenol by metallic nanoparticles immobilized in spherical polyelectrolyte brushes. *J. Phys. Chem. C* **2010**, *114*, 8814–8820. [[CrossRef](#)]
92. Gu, S.; Kaiser, J.; Marzun, G.; Ott, Lu, A.Y.; Ballauff, M.; Zacccone, A.; Barcikowski, S.; Wagener, P. Ligand-free gold nanoparticles as a reference material for kinetics modelling of catalytic reduction of 4-nitrophenol. *Catal. Lett.* **2015**, *145*, 1105–1112. [[CrossRef](#)]
93. Nasaruddin, R.R.; Chen, T.; Li, J.; Goswami, N.; Zhang, J.; Yan, N.; Xie, J. Ligands modulate reaction pathway in the hydrogenation of 4-nitrophenol catalyzed by gold nanoclusters. *ChemCatChem* **2018**, *10*, 395–402. [[CrossRef](#)]
94. Kong, X.; Zhu, H.; Chen, C.; Huang, G.; Chen, Q. Insights into the reduction of 4-nitrophenol to 4-aminophenol on catalysts. *Chem. Phys. Lett.* **2017**, *684*, 148–152. [[CrossRef](#)]
95. Kästner, C.; Thünemann, A. Catalytic reduction of 4-nitrophenol using silver nanoparticles with adjustable activity. *Langmuir* **2016**, *32*, 7383–7391. [[CrossRef](#)] [[PubMed](#)]

96. Lara, L.R.S.; Zottis, A.D.; Elias, W.C.; Faggion, D., Jr.; de Campos, C.E.M.; Acuña, J.J.S.; Domingos, J.B. The catalytic evaluation of in situ grown Pd nanoparticles on the surface of Fe<sub>3</sub>O<sub>4</sub>@dextran particles in the p-nitrophenol reduction reaction. *RSC Adv.* **2015**, *5*, 8289–8296. [[CrossRef](#)]
97. Jiang, Z.; Xie, J.; Jiang, D.; Wei, X.; Chen, M. Modifiers-assisted formation of nickel nanoparticles and their catalytic application to p-nitrophenol reduction. *Cryst. Eng. Comm.* **2013**, *15*, 560–569. [[CrossRef](#)]
98. Jin, L.; Zhao, X.; Ye, J.; Qian, X.; Dong, M. MOF-derived magnetic Ni-carbon submicrorods for the catalytic reduction of 4-nitrophenol. *Catal. Commun.* **2018**, *107*, 43–47. [[CrossRef](#)]
99. Lin, F.-H.; Doong, R.-A. Bifunctional Au-Fe<sub>3</sub>O<sub>4</sub> heterostructures for magnetically recyclable catalysis of nitrophenol reduction. *J. Phys. Chem. C* **2011**, *115*, 6591–6598. [[CrossRef](#)]
100. Eley, D.; Rideal, E.K. Parahydrogen Conversion on Tungsten. *Nature* **1940**, *146*, 401–402. [[CrossRef](#)]
101. Khalavka, Y.; Becker, J.; Sönnichsen, C. Synthesis of rod-shaped gold nanorattles with improved plasmon sensitivity and catalytic activity. *J. Am. Chem. Soc.* **2009**, *131*, 1871–1875. [[CrossRef](#)]
102. Panacek, A.; Pucek, R.; Hrbac, J.; Nevecna, T.; Steffkova, J.; Zboril, R.; Kvitek, L. Polyacrylate-assisted size control of silver nanoparticles and their catalytic activity. *Chem. Mater.* **2014**, *26*, 1332–1339. [[CrossRef](#)]
103. Xu, W.; Kong, J.S.; Yeh, Y.-T.E.; Chen, P. Single-molecule nanocatalysis reveals heterogeneous reaction pathways and catalytic dynamics. *Nat. Mater.* **2008**, *7*, 992–996. [[CrossRef](#)] [[PubMed](#)]
104. Zhou, X.; Xu, W.; Liu, G.; Panda, D.; Chen, P. Size-dependant catalytic activity and dynamics of gold nanoparticles at the single-molecule level. *J. Am. Chem. Soc.* **2010**, *132*, 138–146. [[CrossRef](#)] [[PubMed](#)]
105. Ansar, S.M.; Kitchens, C.L. Impact of gold nanoparticle stabilizing ligands on the colloidal catalytic reduction of 4-nitrophenol. *ACS Catal.* **2016**, *6*, 5553–5560. [[CrossRef](#)]
106. Mei, Y.; Sharma, G.; Lu, Y.; Ballauff, M.; Drechsler, M.; Irrgang, T.; Kempe, R. High catalytic activity of platinum nanoparticles immobilized on spherical polyelectrolyte brushes. *Langmuir* **2005**, *21*, 12229–12234. [[CrossRef](#)] [[PubMed](#)]
107. Lu, Y.; Mei, Y.; Walker, R.; Ballauff, M.; Drechsler, M. ‘Nano-tree’-type spherical polymer brush particles as templates for metallic nanoparticles. *Polymer* **2006**, *47*, 4985–4995. [[CrossRef](#)]
108. Mei, Y.; Lu, Y.; Polzer, F.; Ballauff, M. Catalytic activity of palladium nanoparticles encapsulated in spherical polyelectrolyte brushes and core-shell microgels. *Chem. Mater.* **2007**, *19*, 1062–1069. [[CrossRef](#)]
109. Kalekar, A.M.; Sharma, K.K.K.; Lehoux, A.; Audonnet, F.; Remita, H.; Saha, A.; Sharma, G.K. Investigation into catalytic activity of porous platinum nanostructures. *Langmuir* **2013**, *29*, 11431–11439. [[CrossRef](#)]
110. Menumorov, E.; Hughes, R.A.; Neretina, S. Catalytic reduction of 4-nitrophenol: A quantitative assessment of the role of dissolved oxygen in determining the induction time. *Nano Lett.* **2016**, *16*, 7791–7797. [[CrossRef](#)]
111. Farhadi, S.; Kazem, M.; Siadatnasab, F. NiO nanoparticles prepared via thermal decomposition of the bis(dimethylglyoximate)nickel(II) complex: A novel reusable heterogeneous catalyst for fast and efficient microwave-assisted reduction of nitroarenes with ethanol. *Polyhedron* **2011**, *30*, 606–613. [[CrossRef](#)]
112. Li, M.; Chen, G. Revisiting catalytic model reaction p-nitrophenol/NaBH<sub>4</sub> using metallic nanoparticles coated on polymeric spheres. *Nanoscale* **2013**, *5*, 11919–11927. [[CrossRef](#)]
113. Cho, K.Y.; Seo, H.Y.; Yeom, Y.S.; Kumar, P.; Lee, A.S.; Baek, K.-Y.; Yoon, H.G. Stable 2D-structured supports incorporating ionic block copolymer-wrapped carbon nanotubes with graphene oxide toward compact decoration of metal nanoparticles and high-performance nano-catalysis. *Carbon* **2016**, *105*, 340–352. [[CrossRef](#)]
114. Hwang, J.; Siddique, A.B.; Kim, Y.J.; Lee, H.; Maeng, J.H.; Ahn, Y.; Lee, J.S.; Kim, H.S.; Lee, H. Ionic cellulose-stabilized gold nanoparticles and their application in the catalytic reduction of 4-nitrophenol. *RSC Adv.* **2018**, *8*, 1758–1763. [[CrossRef](#)]
115. Ballarin, B.; Barreca, D.; Boanini, E.; Bonansegna, E.; Cassani, M.C.; Carraro, G.; Fazzini, S.; Mignani, A.; Nanni, D.; Pinelli, D. Functionalization of silica through thiol-yne radical chemistry: A catalytic system based on gold nanoparticles support on amino-sulfide-branched silica. *RSC Adv.* **2016**, *6*, 25780–25788. [[CrossRef](#)]
116. Wang, J.; Wu, Z.; Li, T.; Ye, J.; Shen, L.; She, Z.; Liu, F. Catalytic PVDF membrane for continuous reduction and separation of p-nitrophenol and methylene blue in emulsified oil solution. *Chem. Eng. J.* **2018**, *334*, 579–586. [[CrossRef](#)]
117. Javaid, R.; Ksawasaki, S.-i.; Suzuki, A.; Suzuki, T.M. Simple and rapid hydrogenation of p-nitrophenol with aqueous formic acid in catalytic flow reactors. *Beilstein J. Org. Chem.* **2013**, *9*, 1156–1163.

118. Huang, R.; Zhu, H.; Su, R.; Qi, W.; He, Z. Catalytic membrane reactor immobilized with alloy nanoparticle-loaded protein fibrils for continuous reduction of 4-nitrophenol. *Environ. Sci. Technol.* **2016**, *50*, 11263–11273. [[CrossRef](#)]
119. Srivastava, A.K.; Mondal, K.; Mukhopadhyay, K.; Prasad, N.E.; Sharma, A. Facile reduction of para-nitrophenol: Catalytic efficiency of silver nanoferns in batch and continuous flow reactors. *RSC Adv.* **2016**, *6*, 113981–113990. [[CrossRef](#)]
120. Xu, D.; Wang, F.; Yu, G.; Zhao, H.; Yang, J.; Yuan, M.; Zhang, X.; Dong, Z. Animal-based hypercrosslinked polymer modified with small palladium nanoparticles for efficiently catalytic reduction of nitroarenes. *ChemCatChem* **2018**, *10*, 4569–4577. [[CrossRef](#)]
121. Liu, Y.; Guerrouache, M.; Kebe, S.I.; Carbonnier, B.; Le Droumaguet, B. Gold nanoparticles-supported histamine-grafted monolithic capillaries as efficient microreactors for flow-through reduction of nitro-containing compounds. *J. Mater. Chem. A* **2017**, *5*, 11805–11814. [[CrossRef](#)]
122. Wu, X.-Q.; Wu, X.-W.; Shen, J.-S.; Zhang, H.-W. In situ formed metal nanoparticle systems for catalytic reduction of nitroaromatic compounds. *RSC Adv.* **2014**, *4*, 49287–49294. [[CrossRef](#)]
123. Wu, X.-Q.; Wu, X.-W.; Huang, Q.; Shen, J.-S.; Zhang, H.-W. In situ synthesized gold nanoparticles in hydrogels for catalytic reduction of nitroaromatic compounds. *Appl. Surf. Sci.* **2015**, *331*, 210–218. [[CrossRef](#)]
124. Tsao, Y.-C.; Rej, S.; Chiu, C.-Y.; Huang, M.H. Aqueous phase synthesis of Au-Ag core-shell nanocrystals with tunable shapes and their optical and catalytic properties. *J. Am. Chem. Soc.* **2014**, *136*, 396–404. [[CrossRef](#)] [[PubMed](#)]
125. Shultz, L.R.; Hu, L.; Preradovic, K.; Beazley, M.J.; Feng, X.; Jurca, T. A broader-scope analysis of the catalytic reduction of nitrophenols and azo dyes with noble metal nanoparticles. *ChemCatChem* **2019**, *11*, 2590–2595. [[CrossRef](#)]

**Sample Availability:** Not available.



© 2019 by the authors. Licensee MDPI, Basel, Switzerland. This article is an open access article distributed under the terms and conditions of the Creative Commons Attribution (CC BY) license (<http://creativecommons.org/licenses/by/4.0/>).